Supporting Information

Boosting CO_2-to-CO Conversion on a Robust Single-Atom Copper Decorated Carbon Catalyst by Enhancing Intermediate Binding Strength

Shixia Chen, [a‡] Yuewei Li, [a‡] Zhuogang Bu, [a] Fangqi Yang, [a] Junhui Luo, [a] Qizheng An, [b] Zheling Zeng [a], Jun Wang, *[a] and Shuguang Deng *[c]

[a]School of Resources Environmental & Chemical Engineering, Nanchang University, Nanchang, 330031, China

[b]School of Material Science and Engineering and Institute for Advanced Study, Nanchang University, Nanchang, 330031 P. R. China

[c]School for Engineering of Matter, Transport and Energy, Arizona State University, 551 E. Tyler Mall, Tempe, AZ 85287, USA

[‡] These authors contributed equally to this work.

*Corresponding authors:

1. E-mail: shuguang.deng@asu.edu (S. Deng)

2. E-mail: jwang7@ncu.edu.cn (J. Wang)

Table of contents

Experimental Section

1. Catalyst Synthesis.

1.1 Materials and chemicals.

Zinc nitrate hexahydrate ($Zn(NO_3)_2 \cdot 6H_2O$, >99%) and methanol (MeOH) were purchased from XiLONG SCIENTIFIC Co., Ltd (China). 2-Methyl imidazole (2-MeIM, 99%), Phthalocyanine copper (CuPc), copper nitrate trihydrate, and cobalt nitrate hexahydrate were purchased from Aladdin. Nafion solution (5 wt%) was purchased from Du Pont. All reagents were commercially purchased and used as received without further purification.

1.2 Synthesis of Cu-N-C and N-C.

In a typical synthesis procedure, 0.338 g $Cu(NO_3)_2 \cdot 3H_2O$ (1.4 mmol) and 3.332 g $Zn(NO_3)_2 \bullet 6H_2O$ (11.2 mmol) in 125mL methanol (molar ratio of copper and zinc was 1:8) was poured into 125 mL methanol solution of 1.617 g 2-MeIM (19.7 mmol). This mixture solution was magnetically stirred at room temperature for 48 h. The products were collected by centrifugation and washed by methanol for at least three times. The products were dried at 60 ℃ overnight in a drying oven and named as Cu/Zn-ZIF. Similarly, the synthesis of N-C was according to the same procedures except that only 12.6 mM $Zn(NO_3)_2 \bullet 6H_2O$ was added to the mixed solution.

The above-synthesized Cu/Zn-ZIF and ZIF-8 were used as precursors and transferred into a tube furnace, heated to 1000 ℃ under Ar for 2 h. After carbonization, the resultants were washed thoroughly in a 1.0 M HCl aqueous solution at 80 ℃ for 10 h to remove residual metal nano-particles and Zn species. After drying in vacuum at 60 ℃ overnight, Cu-N-C and N-C were thus obtained.

1.3 Optimization of synthesis condition.

In order to investigate the effect of Cu contents on the CO_2RR performances, Cu-N-C catalysts with different Cu/Zn ratios (denoted as Cu-N-C-x, where x represents the molar ratio of Cu/Zn) were also prepared and tested under the same conditions. The CO and H_2 are the main products as well. The CO FEs were measured to be 80.5% and 90% on Cu-N-C-6 and Cu-N-C-10, respectively (Figure. S21), which are both lower than that of Cu-N-C. Thus, the Cu/Zn ratio of 8 was selected as the optimized synthesis condition.

2. Physicochemical characterization.

The morphologies of catalysts were characterized by the scanning electron microscopy (SEM, HIT SU1510) and high-resolution transmission electron microscopy (HRTEM, FEI Quanta 200). Energy dispersive X-ray spectroscopy (EDS) images were collected by INCA 6650 (Oxford Instrument, UK, for low-resolution images). The high-angle annular dark-field scanning transmission electron microscopy (HAADF-STEM) was performed on a Thermo Titan Themmis AC-STEM, 60-300"cubed" microscope fitted with aberration-correctors for the imaging lens and the probe forming lens, operated at 300 kV. The crystal structures of the catalysts were studied by powder X-ray diffraction (XRD) using Panalytical Empyrean diffractometer with Cu-Kα radiation. Raman spectra were collected using an HR Evolution Raman microscope. X-ray photoelectron spectroscopy (XPS) measurements were performed on the Thermo Scientific ESCALAB 250Xi. The Cu contents in the catalysts were measured by inductively coupled plasma mass spectrometry (ICP-MS, Varian 820-MS). N_2 adsorption-desorption were measured at 77 K using a Micromeritics ASAP 2460 instrument with degassing samples under vacuum at 423 K for 15 h. The specific surface areas of the catalysts were determined by the Brunauer Emmett Teller (BET) equation. CO_2 adsorption-desorption isotherms were measured at 273, 298, and 323 K using a Micromeritics ASAP 2460 instrument with degassing samples under vacuum at 423 K for 15 h. Liquid-phase reduction products were analyzed with 1H NMR spectra using an Ascend 400 spectrometer (400 MHz, Bruker).

The X-ray absorption spectroscopy (XAS) measurements at Cu K (E_0=8983 eV)

edge were collected on the beamline BL01C1 in NSRRC. The energy was calibrated accordingly to the absorption edge of pure Cu foil. The radiation was monochromatized by a Si (111) double-crystal monochromator. XANES and EXAFS data reduction and analysis were processed by Athena software. The chemical valence of Cu in the samples was determined by the comparison with the reference Cu foil, Cu_2O, CuO and CuPc. For the extended X-ray absorption fine structure (EXAFS) part, the Fourier transformed (FT) data in R space were analyzed by applying the first-shell approximate model for Cu-N contribution. The passive electron factor S_0^2 was determined by fitting the experimental data on Cu foil and then fixed for future analysis of the measured samples.

3. Electrochemical Measurements.

Electrocatalytic CO_2RR measurements were carried out in a two-compartment three-electrode electrochemical cell separated by Nafion 115 in CO_2-saturated 0.5 M $KHCO_3$ electrolyte (pH=7.2), and the cell was connected with an electrochemical station (CHI660E). A Pt foil (2 × 2 cm) and saturated Ag/AgCl were utilized as the counter and reference electrode, respectively. The working electrode was prepared by drop-casting 100 μL of catalyst ink onto carbon paper (1 cm^{-2}) with a mass loading of 1.90 mg cm^{-2}. The ink was prepared by dispersing 5 mg catalyst and 5 mg carbon black in a mixture solution of 500 μL ethanol, and 25 μL 5% Nafion solution via sonication for 2 h. The catalyst loading was about 0.95 mg cm^{-2}. The working electrode is placed in the cathode chamber separated from the anode chamber by a piece of Nafion 115 ionic exchange membrane. The high purity CO_2 was introduced in the cathode chamber for 1 h with a flow rate of 20 mL min^{-1} before electrolysis. The gas-phase products were analyzed by using an online gas chromatograph (Agilent 7890B) equipped with Al_2O_3 column and HaysepQ column and with a thermal conductivity detector (TCD) for H_2 and CO quantification, while a flame ionization detector (FID) for C_2H_4 and C_2H_6 quantification. Ultra pure helium (He, 99.9999%) was used as the carrier gas. The liquid products were quantified by nuclear magnetic resonance (NMR) (Bruker AV 600Mhz) spectroscopy. All potentials in this study were measured against the Ag/AgCl reference electrode and converted to the RHE reference scale using E (vs. RHE) = E (vs.

Ag/AgCl) + 0.21 V + 0.0591×pH.

Flow cell configuration was consisted of a Cu-N-C loaded gas diffusion layer (GDL, 1 mg cm^{-2}, 2 × 2 cm^2) as the cathode, a piece of anion exchange membrane (Nafion, 2 × 2 cm^2) as the separator, a Ti/IrO_2 electrode (2 × 2 cm^2) as the anode, and 1M KOH as the catholyte. The Ag/AgCl (in saturated KCl) was as the reference electrode. The work electrode area was controlled around 1 cm^2. During the measurements, CO_2 gas was directly fed to the cathode GDL controlled at a rate of 20 ml min^{-1} by a mass flow controller.

The Faradic efficiency calculation was based on the definition of Faradic efficiency:[1]

$$f_i = \frac{Q_i}{Q_{total}} \tag{1}$$

where *i* represents CO, H_2 or CH_4.Q_i and Q_{total} can be obtained from the following equations:

$$Q_i = Z_i \times F \times N_i \tag{2}$$

$$Q_{total} = I \times t \tag{3}$$

Based on the GC data and ideal gas law:

$$N_i = N_{total} \times V_i \tag{4}$$

$$N_{total} = \frac{P_O \times V_O}{R \times T_O} \tag{5}$$

$$V_O = G \times t \tag{6}$$

where *G* is the volumetric flow rate.

So, equation (1) can be written as:

$$FE = \frac{Z_i \times V_i \times G \times F \times P_O}{I \times R \times T_O \times 60,000} \tag{7}$$

Q_i: the charge used for the reduction of a certain product, C

Q_{total}: the charge passed, C

Z_i: the number of electrons exchanged for product formation, which is 2 for H_2 and

CO

F: Faradaic constant, which is 96485 C mol^{-1}

N_i: moles of product i in the GC sampling loop, mol

I: the average current in a period (t) of electrocatalysis:

$$I = \frac{\int_0^t I(t)dt}{t} \quad (8)$$

t: time for gas to fill the GC sampling loop;

N_{total}: moles of all gases in the GC sampling loop;

V_i: the volume ratio of product i in the GC sampling loop,

P_0 : atmospheric pressure (1.013×10^5 Pa);

V_O: volume of the GC sampling loop;

R: ideal gas constant(8.314 J mol^{-1} K^{-1})

T: reaction temperature (298 K);

TOF for CO production was calculated as following:[2]

$$TOF = \frac{I_{product} / nF}{m_{cat} \times \omega / M_{mental}} \times 3600 \quad (9)$$

$I_{product}$: partial current for CO, A;

n: the number of electrons transferred for CO production (2 in this case);

F: Faradaic constant, 96485C mol^{-1};

m_{cat}: the mass of catalyst on the electrode, g;

ω: metal loading in the catalyst based on ICP-MS results;

M_{metal}: atomic mass of Cu (63.54 g mol^{-1}) for Cu-N_6;

4. Density Functional Theory (DFT) Calculation method.

The present first principle DFT calculations are performed by the Vienna Ab initio Simulation Package (VASP)[3] with the projector augmented wave (PAW) method.[4] The exchange-functional is treated using the generalized gradient approximation (GGA) of Perdew-Burke-Ernzerhof (PBE)[5] functional. The valence electron configurations applied in this work are $2s^22p^2$ (C), $2s^22p^3$ (N) and $3d^{10}4s^1$(Cu), respectively. The energy cut off for the plane wave basis expansion was set to 450 eV and the force on each atom less than 0.03 eV/Å was set for convergence criterion of geometry relaxation.

For the single-Cu defective graphene systems, 5×5×1 supercell containing 49 atoms are applied. The Brillouin zone integration is performed using 3×3×1 Monkhorst and Pack[6] k-point sampling through all the computational process. The self-consistent calculations apply a convergence energy threshold of 10^{-4} eV.

The free energy of hydrogen adsorption (ΔG*H) can be calculated as followed:[7]

$$\Delta G*H = \Delta E + 0.24eV \quad (10)$$

In this work, CO2 reduction was considered as followed:

$$* + CO_2 + H^+ + e^- \rightarrow *COOH \quad (11)$$

$$*COOH + H^+ + e^- \rightarrow *CO \quad (12)$$

$$*CO \rightarrow * + CO \quad (13)$$

Here, the asterisk (*) represents the surface substrate active site (Cu-N_4, Cu-N_3, and N-C structures). The free energies of the CO_2 reduction steps (CO_2RR) were calculated by the equation:[8] $\Delta G=\Delta EDFT+\Delta EZPE-T\Delta S$, where ΔEDFT is the DFT electronic energy difference of each step, ΔEZPE and ΔS are the correction of zero-point energy and the variation of entropy, respectively, which are obtained by vibration analysis, T is the temperature (T = 300 K).

The adsorption energy of CO_2 was calculated according to the following equation：

$$E_{ads} = E_{total} - E_{sub} - E_{CO2} \quad (14)$$

where E_{total} is the total energy of the CO_2 adsorbed on the substrate, E_{sub} and E_{CO2} are the energies of the clean substrate and the CO_2 molecule, respectively.

The formation energy of catalysts were calculated using the following equation:

$$E_f = E_{tot} - E_{graphene} + n\mu_C - m\mu_N - \mu_{Cu} \quad (15)$$

where n and m represent the number of carbon defects and nitrogen in catalysts; E is the total energy of each system; and μ_C, μ_N, and μ_{Cu} are the chemical potential of carbon, nitrogen, and Cu defined as the total energy per atom in pristine graphene, nitrogen gas, and Cu bulk metals, respectively.

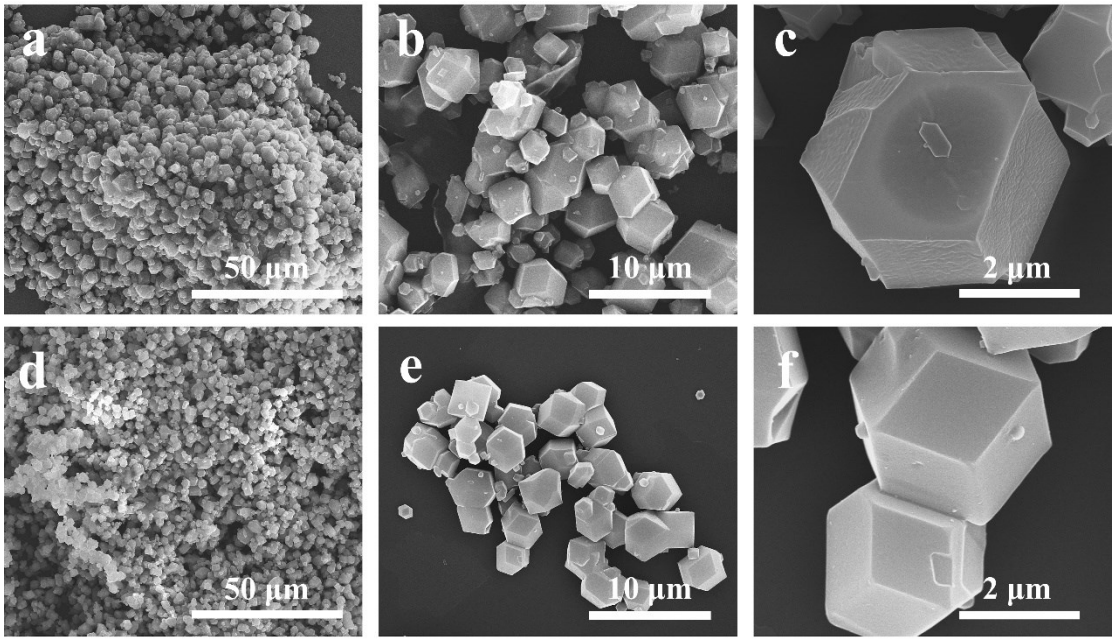

Figure S1. (a-c) SEM images of Cu/Zn-ZIF and (d-f) ZIF-8.

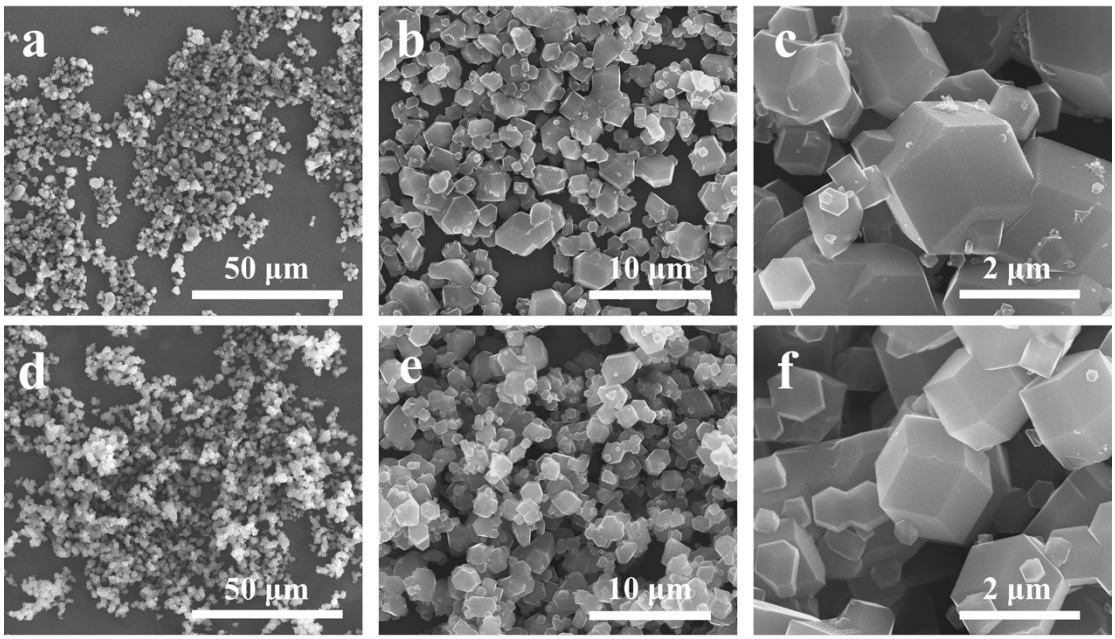

Figure S2. (a-c) SEM images of Cu-N-C and (d-f) N-C.

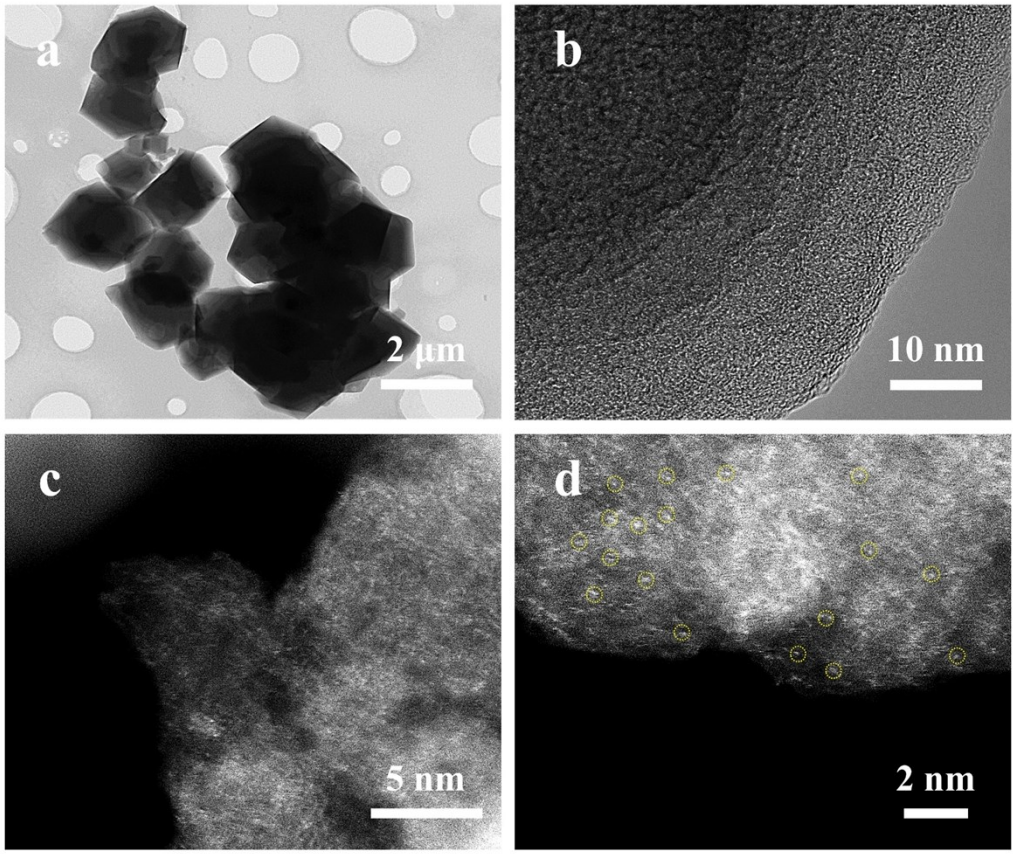

Figure S3. (a, b) The HR-TEM and (c, d) HAADF-STEM images of Cu-N-C from different regions.

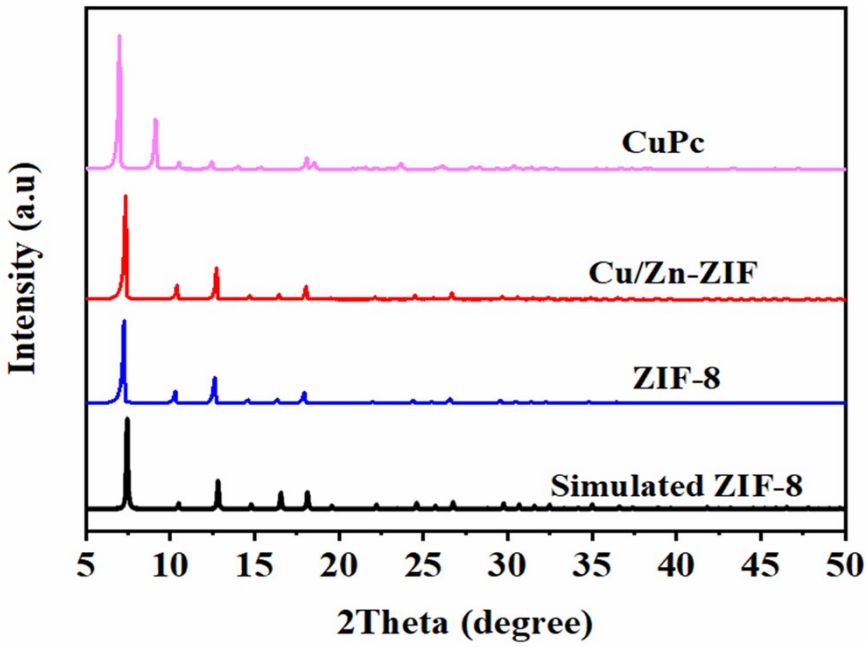

Figure S4. The powder X-ray diffraction patterns of Cu phthalocyanine (CuPc), Cu/Zn-ZIF, ZIF-8, and simulated ZIF-8.

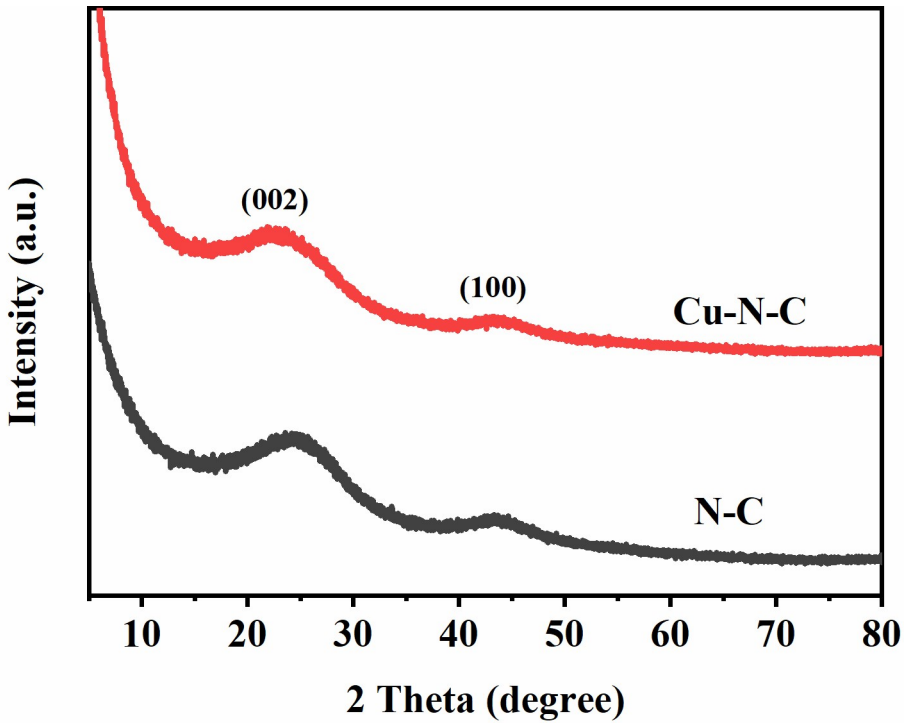

Figure S5. The powder X-ray diffraction patterns of Cu-N-C and N-C catalyst.

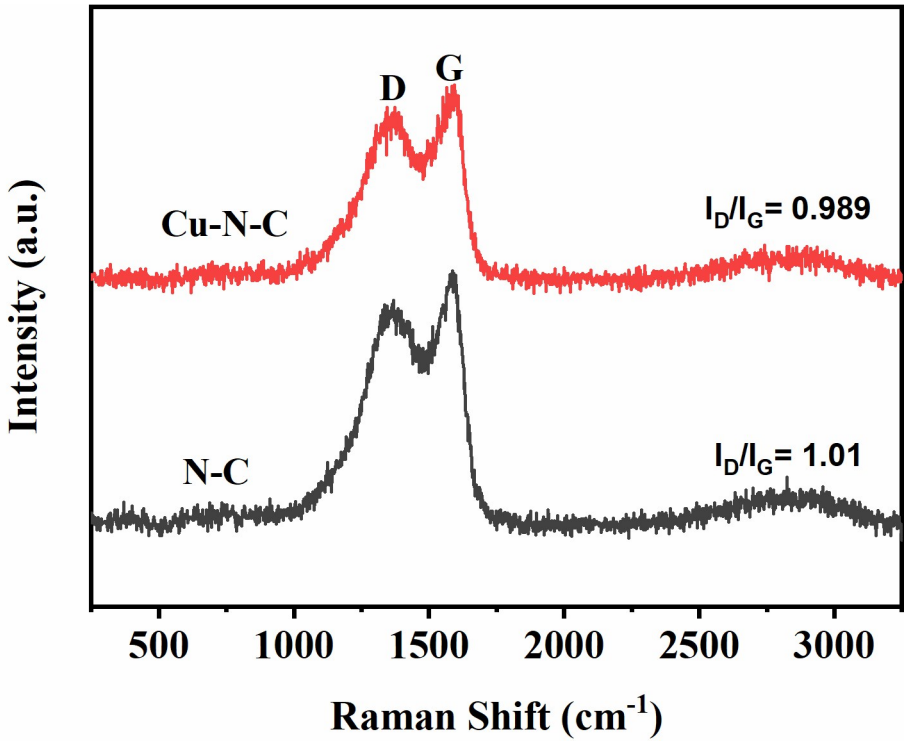

Figure S6. Raman spectra of the Cu-N-C and N-C catalyst.

Table S1. Comparison of Metal Content in Cu-N-C Electrocatalysts determined by XPS and ICP-MS.

Metal content	XPS (at.%)	ICP-MS (wt.%)
Cu	0.12	0.61

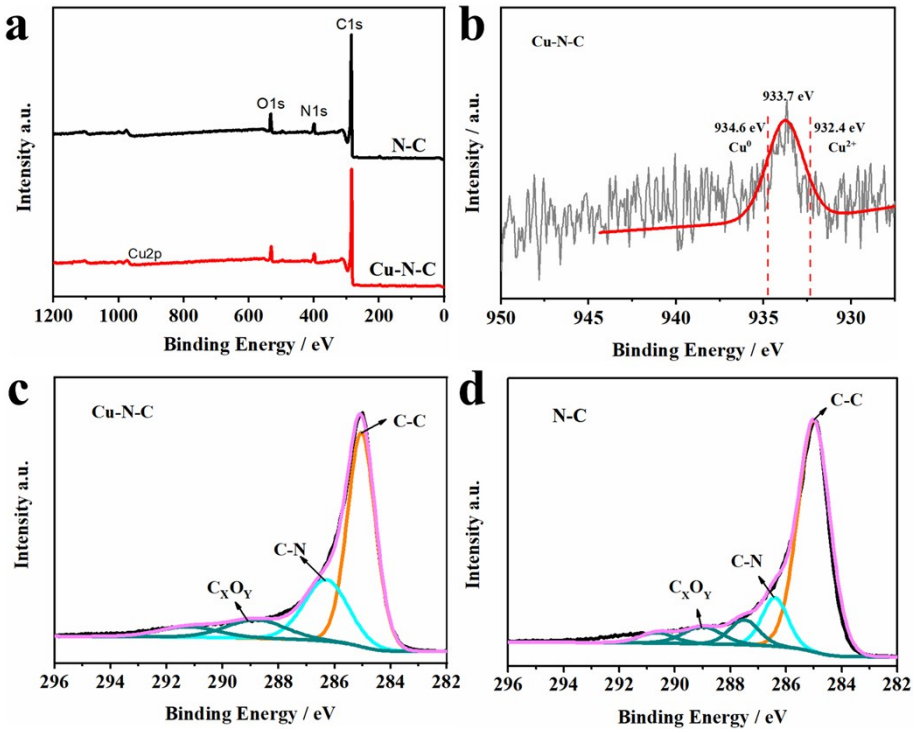

Figure S7. (a) Wide XPS survey and (b) Fitted Cu 2p XPS spectrum of Cu-N-C catalysts; (c,d) XPS C1s spectra of Cu-N-C and N-C.

Table S2. XPS element quantification of catalysts.

Catalyst	C (at%)	N (at%)	O (at%)	Cu (at%)
N-C	87.95	6.17	5.88	/
Cu-N-C	87.31	6.80	5.77	0.12

Table S3. The peak quantification of XPS fitted N1s spectra of catalysts.

Catalyst	Pyridinic N (%)	M-N (%)	Graphitic N (%)	Oxidized N (%)
N-C	39.27	/	53.08	7.65
Cu-N-C	39.47	8.03	43.76	8.74

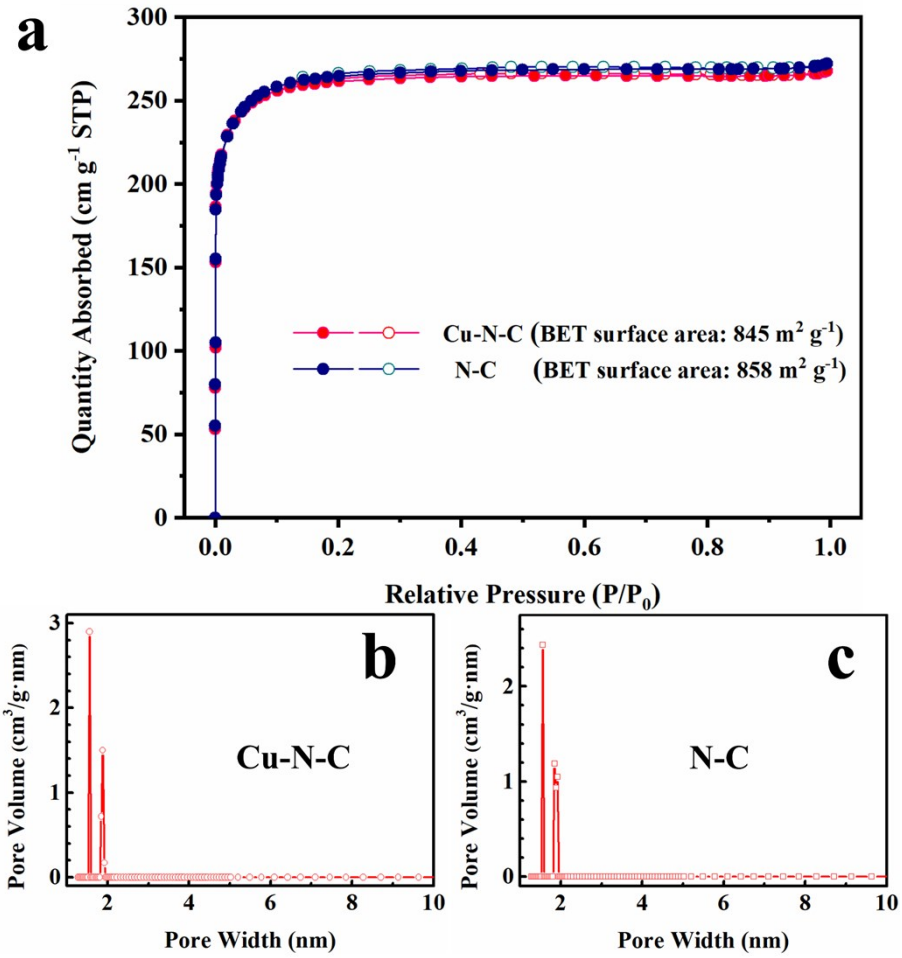

Figure S8. (a) The N_2 sorption isotherms at 77 K and the pore diameter distribution of (b) Cu-N-C and (c) N-C.

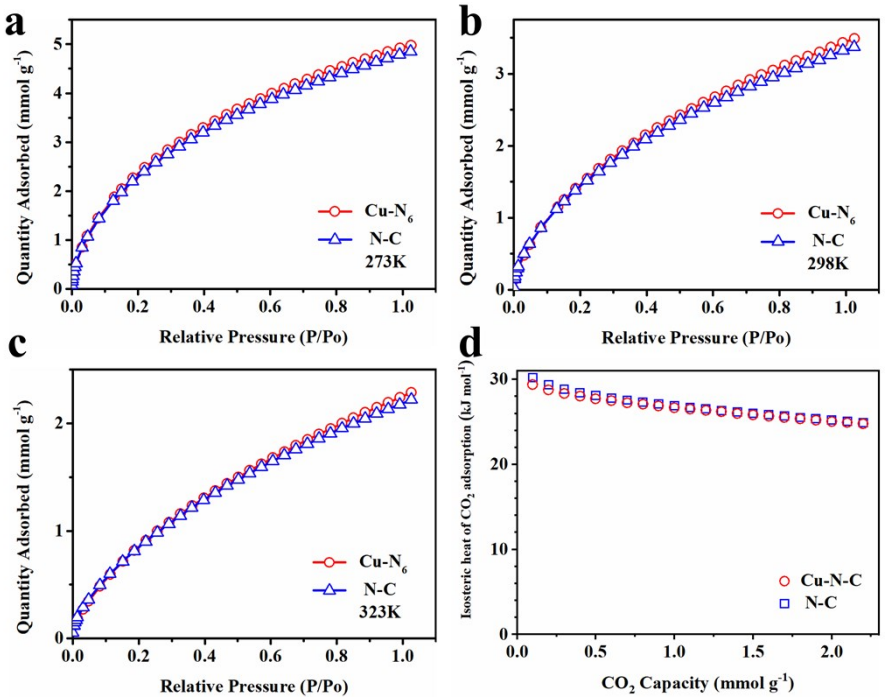

Figure S9. CO_2 adsorption isotherms of N-C and Cu-N-C at (a) 273 K, (b) 298 K, and (c) 323 K; (d) CO_2 isosteric adsorption heat of N-C and Cu-N-C.

Table S4. EXAFS fitting parameters at the Cu K-edge for various samples (S_0^2=0.816)

Sample	1st shell		2st shell		σ^2(Å^2)[c]	ΔE_0(eV)[d]
	R(Å)[b]	N[a]	R(Å)[b]	N[a]		
Cu-N-C	1.90±0.02	3.2±0.2	3.46±0.02	4.5±0.2	0.0028±0.02	-6.1
CuPc	1.95	4.0	/	/	0.0021	9.0
CuO	1.95	4.0	2.93	6.5	0.0049	6.5
Cu_2O	1.85	4.0	3.03	11.2	0.0023	10.7
Cu foil	2.55	12	/	/	0.0088	5.7

[a]N: coordination numbers; [b]R: bond distance; [c]σ^2: Debye-Waller factors; [d] ΔE_0: the inner potential correction. R factor: goodness of fit. S_0^2 was set to 0.816, according to the experimental EXAFS fit of Cu foil by fixing CN as the known crystallographic value.

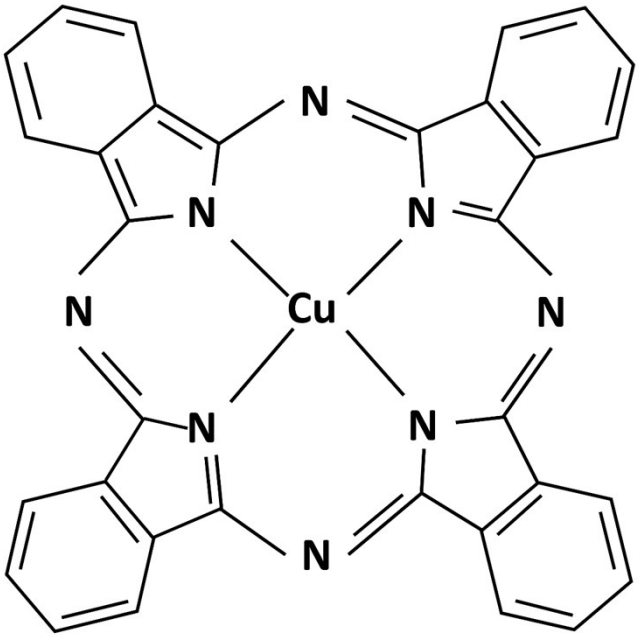

Figure S10. Schematic chemical structure of Cu phthalocyanine (CuPc), where four Cu-N bonds are present and used as the reference for the chemical environment of Cu-N-C catalyst.

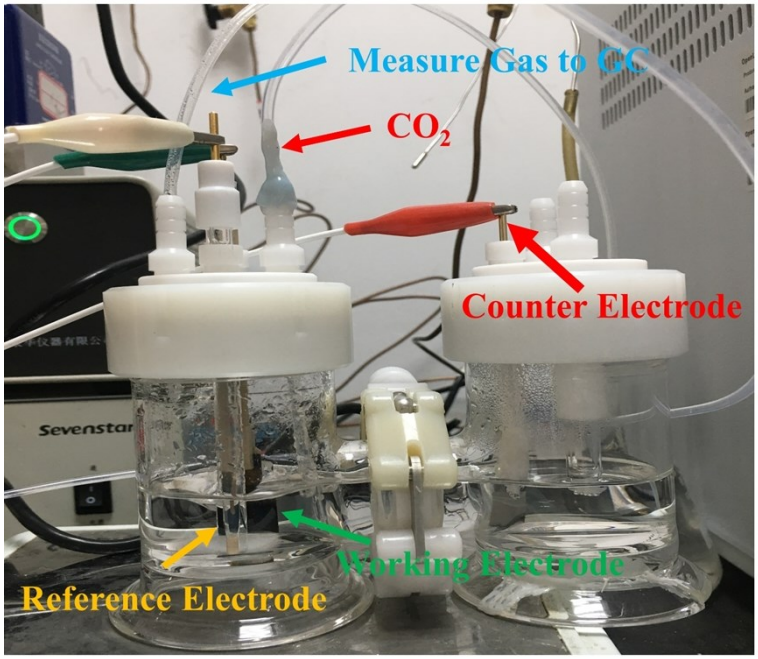

Figure S11. Photograph of the H-type electrochemical cell for CO_2 reduction reactions.

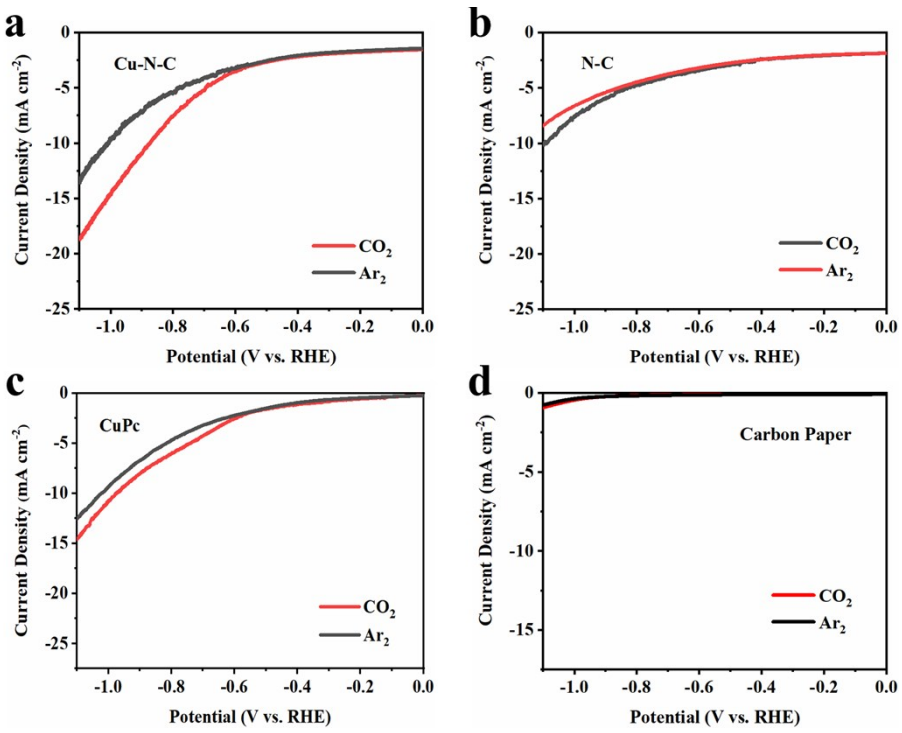

Figure S12. The LSV curves of catalysts in Ar- and CO_2-saturated 0.5 M $KHCO_3$ electrolyte at a scan rate of 5 mV s^{-1}.

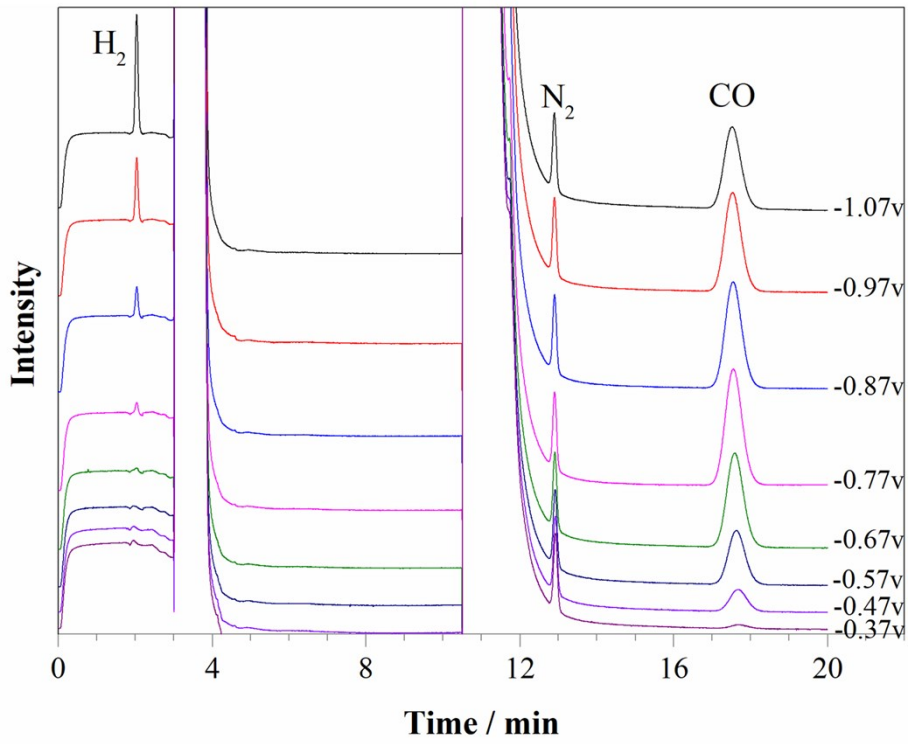

Figure S13. GC plots of the gas products at different potential on Cu-N-C catalyst.

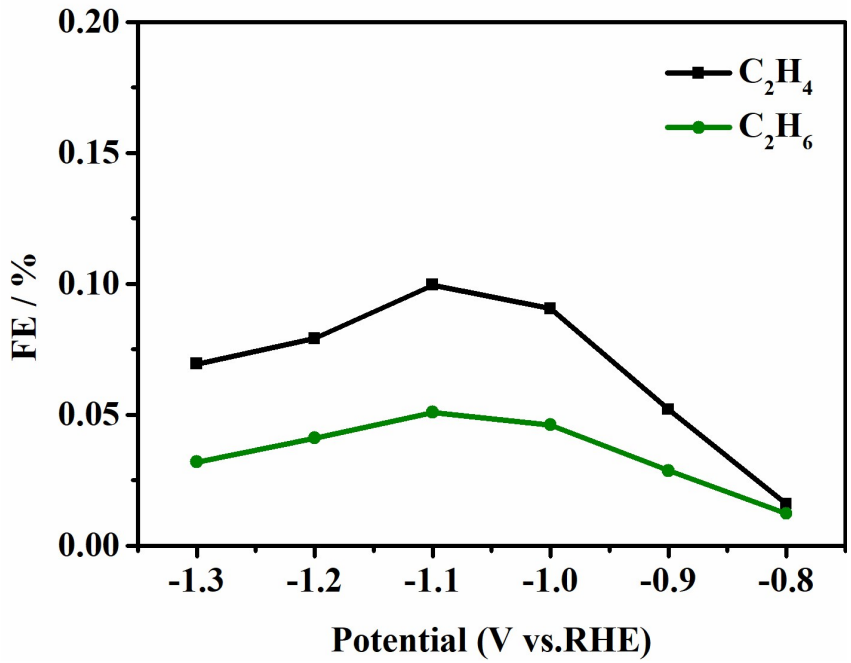

Figure S14. C_2H_4 and C_2H_6 FEs of Cu-N-C.

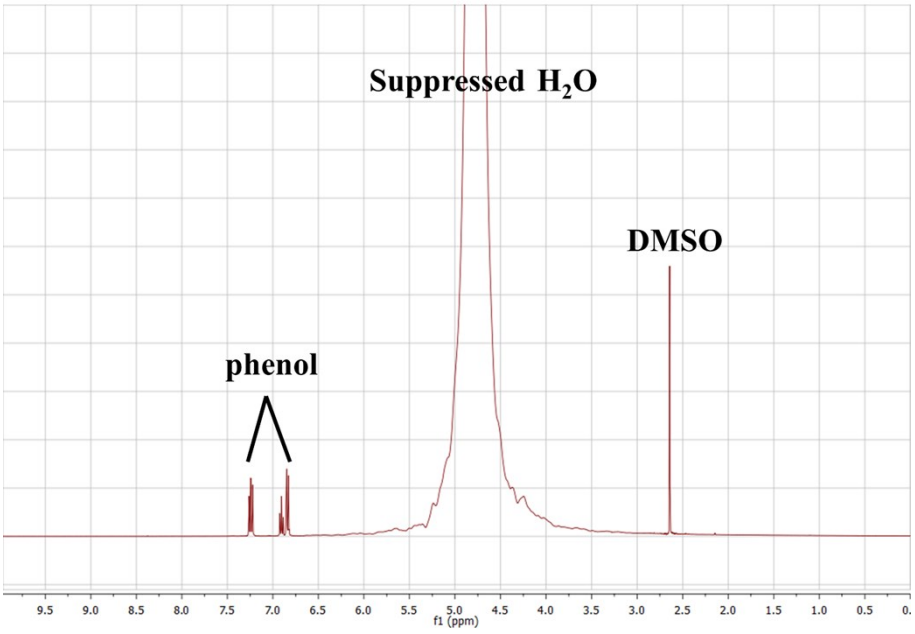

Figure S15. The NMR spectra of potential liquid products at -0.77 V for 2 h.

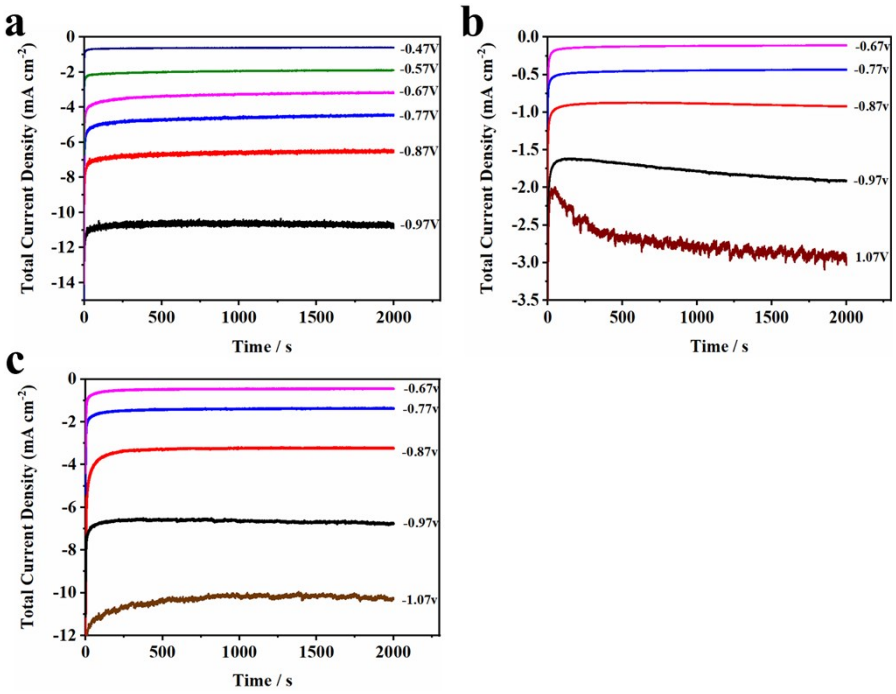

Figure S16. 2000 seconds continuous chronoamperometric experiments for CO_2RR at different applied potentials on (a) Cu-N-C, (b) N-C, and (c) CuPc.

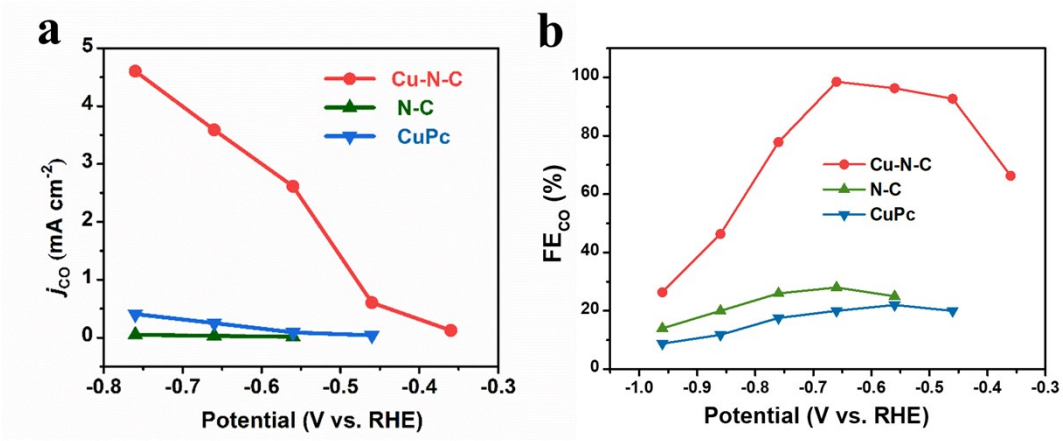

Figure S17. (a) j_{CO} and (b) CO FE of Cu-N-C, N-C, and CuPc.

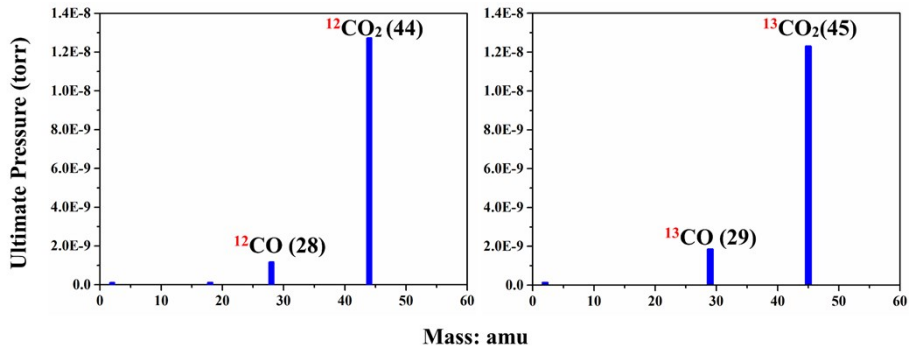

Figure S18. ^{13}C isotope labeling experiments at -0.67 V on Cu-N-C for CO_2RR.

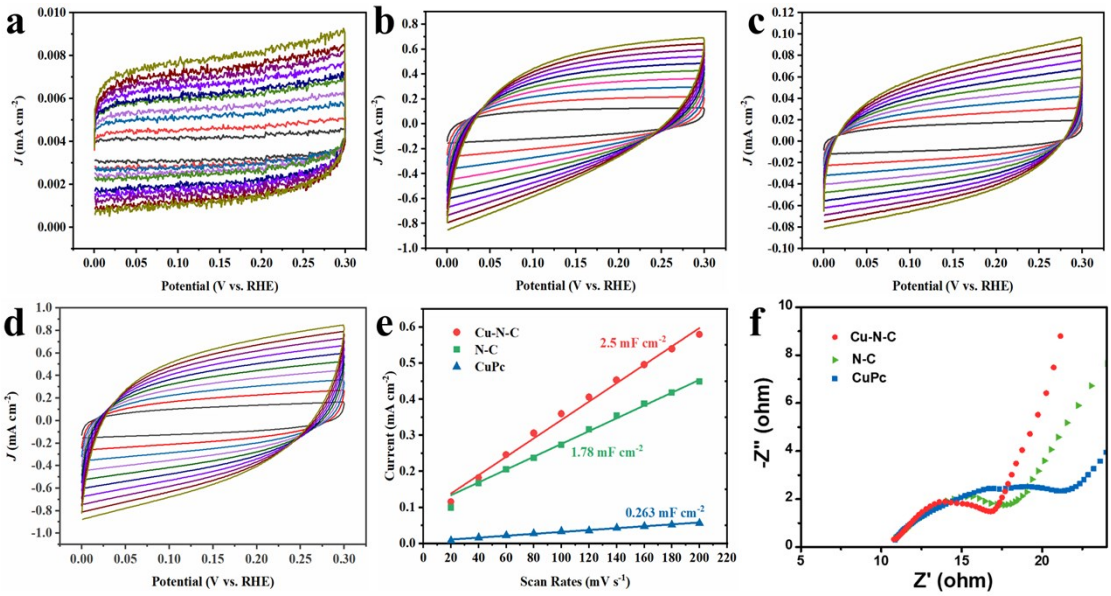

Figure S19. (a-d) The electrochemical capacitance measurements of carbon paper, N-C, CuPc, and Cu-N-C; (e) Electrochemically active surface areas estimated from the double-layer capacitances; (f) Electrochemical impedance spectroscopy of obtained samples.

Electrochemical surface area (ECSA): ECSA was determined for all catalyst studied here opting the well-known double layer capacitance method (C_{dl}) after FE tests. The C_{dl} was determined by measuring the capacitive current associated with double-layer charging from the scan-rate dependence of cyclic voltammetric (CV) stripping. So the potential window of CV stripping was 0-0.3 V versus RHE in 0.5 M $KHCO_3$ solution based on the previous reported literatures.[9, 10] The scan rates were 20 to 200 mV s^{-1}. The C_{dl} was estimated by plotting the $\Delta j = (j_a - j_c)$ at 0.15 V (where j_a and j_a are the cathodic and anodic current densities, respectively) versus RHE against

the scan rate, in which the slope was twice that of C_{dl}. The ECSAs were calculated by the following equation: ECSAs = R_fS, where R_f and S represented the roughness factor and surface area of the carbon paper electrode (1 cm^2 in this case), respectively. The value of R_f was positively related to C_{dl}.

Electrochemical impedance spectroscopy (EIS): The semicircular characteristic in the high-frequency region of EIS curves represents the charge transfer resistance (R_{ct}). As shown in Figure S19f, Cu-N-C displays a smaller R_{ct} than that of N-C and CuPc, demonstrating the boosted electron-transfer during CO_2RR.

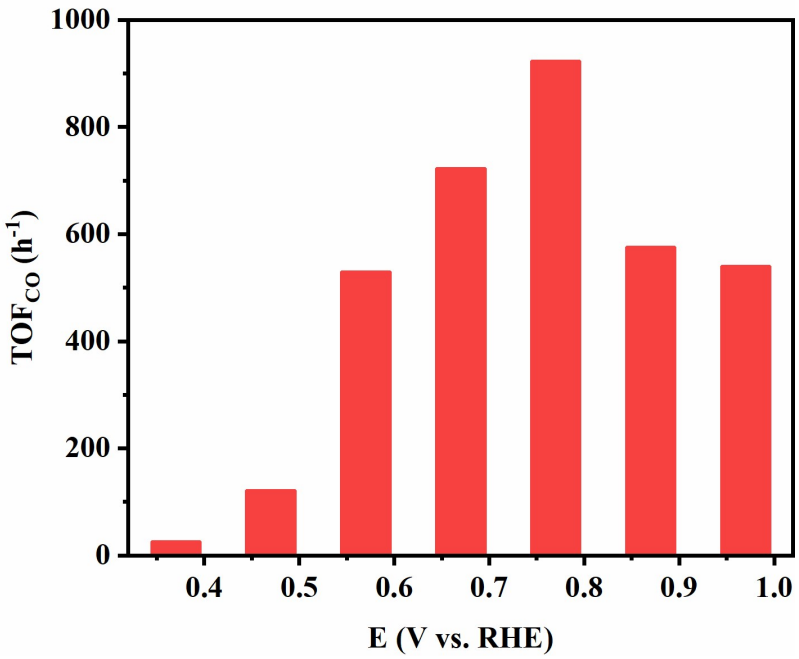

Figure S20. TOF of Cu-N-C at various applied potentials.

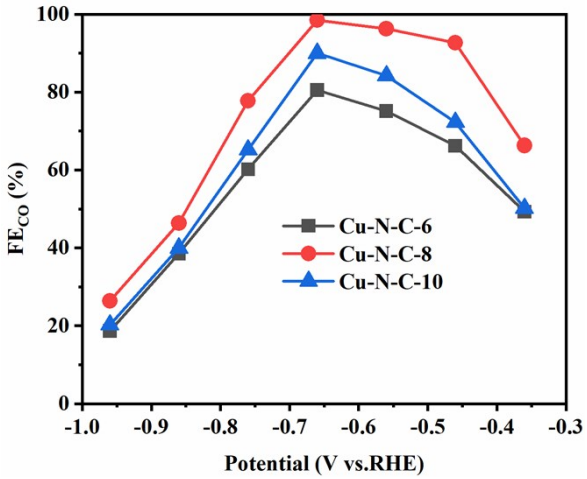

Figure S21. The optimization of CO_2RR activity over Cu-N-C by adjusting Cu/Zn ratios.

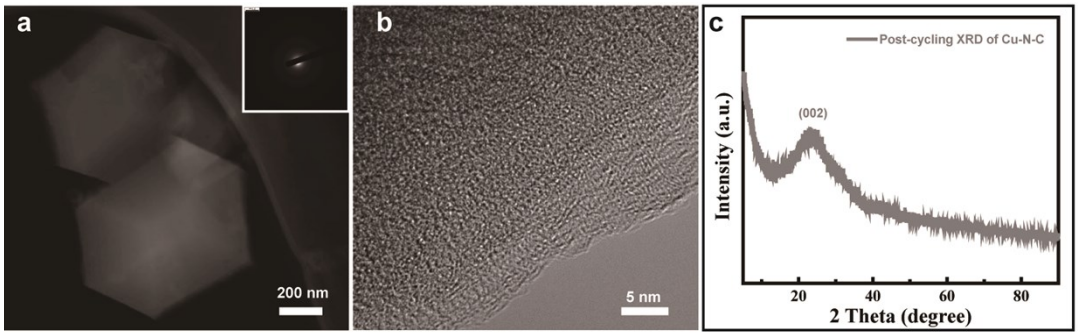

Figure S22. Characterizations of Cu-N-C after continuous electrolysis under – 0.67 V CO_2 to CO overpotential. (a) TEM image and SAED (inset); (b) corresponding HR-TEM; (c) XRD spectra of Cu-N-C.

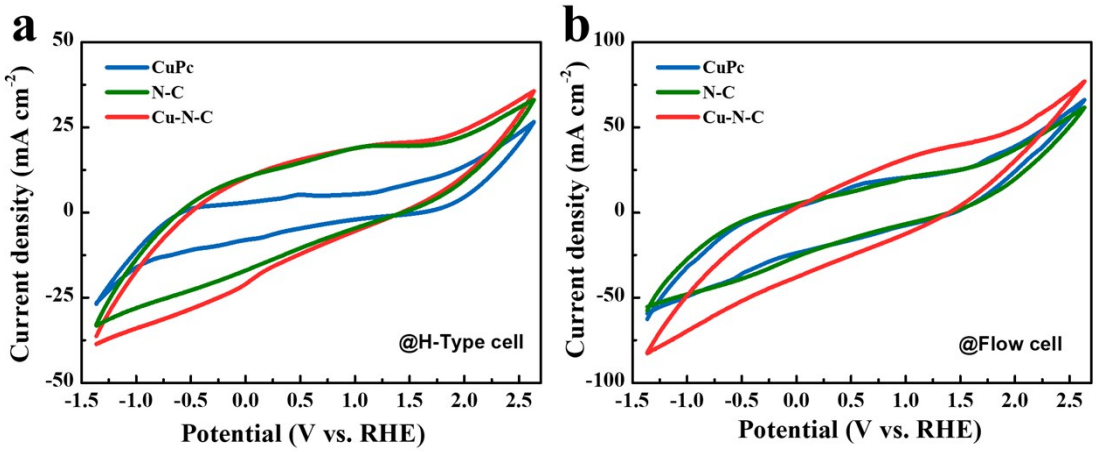

Figure S23. The CV curve within -1.35-2.53 V of CuPc, N-C, and Cu-N-C in (a) H-Type cell and (b) Flow cell.

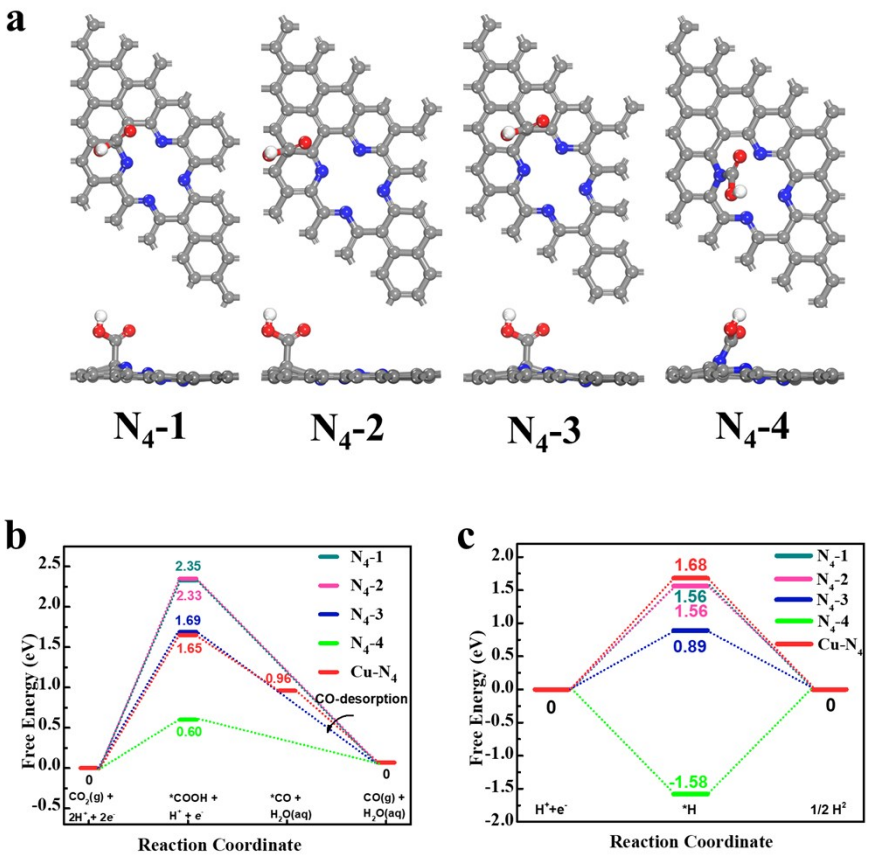

Figure S24. (a) Optimized atomic structures for *COOH intermediates adsorbed on four N4 sites; Calculated Gibbs free energy diagrams for (b) CO_2RR, and (c) HER on Cu-N_4 and N4 sites.

Four N4-C structures (named as N_4-1, N_4-2, N_4-3, and N_4-4) with different adsorbed sites of intermediate states (*COOH) have been constructed based on the DFT (Figure S24a). According to the DFT calculation, the free-energy barrier of *COOH formation on N_4-1, N_4-2, N_4-3, and N_4-4 are 2.33, 2.35, 1.69, and 0.60 eV, respectively, while that on Cu-N_4 is 1.65 eV (Figure S24b), suggesting the strong combination with the *COOH. However, to fully understand the role of N-doped sites for CO2RR, we must also consider the competing HER. As shown in Figure S24c, obviously, all the N4 sites show relatively stronger *H binding due to the lower free energies of *H formation than that of *COOH formation, which leads to extensive H* coverage and therefore hinders CO formation, resulting in low CO Faradaic efficiency. This was consistent with the

experimental results of CO_2RR in Figure S17. In contrast, for the Cu-N_4 system, the energy barrier for HER was calculated to be 1.68 eV, which is higher than that of CO_2RR (1.65 eV), demonstrating the introduction of Cu sites into N-C substrate could effectively suppress the HER and result in high selectivity toward CO_2RR while N-doped sites are the main active sites in HER. Notably, Cu-N3 is not worthy compared due to the unreasonable structure, as proved in Figures 4b and 4c. And the none *CO intermediate states in the CO_2-CO pathway Gibbs free energy diagrams of N4 sites is due to the directly desorption of CO, which was consistent with the previous reported literature.[11]

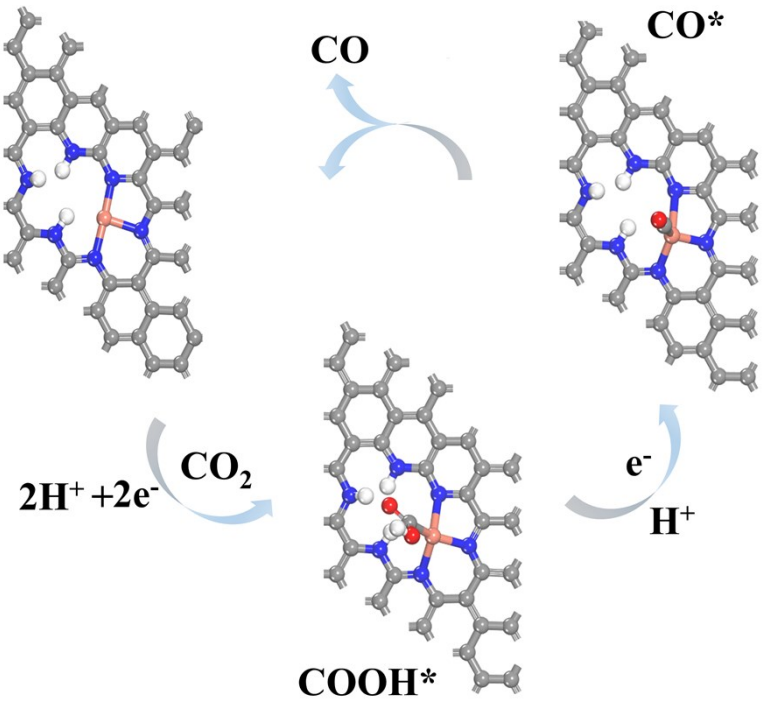

Figure S25. Adsorption configurations for COOH* and CO* during CO2RR. In the figure, the gray, blue, pink, red, and white balls represent C, N, Cu, O, and H atoms, respectively.

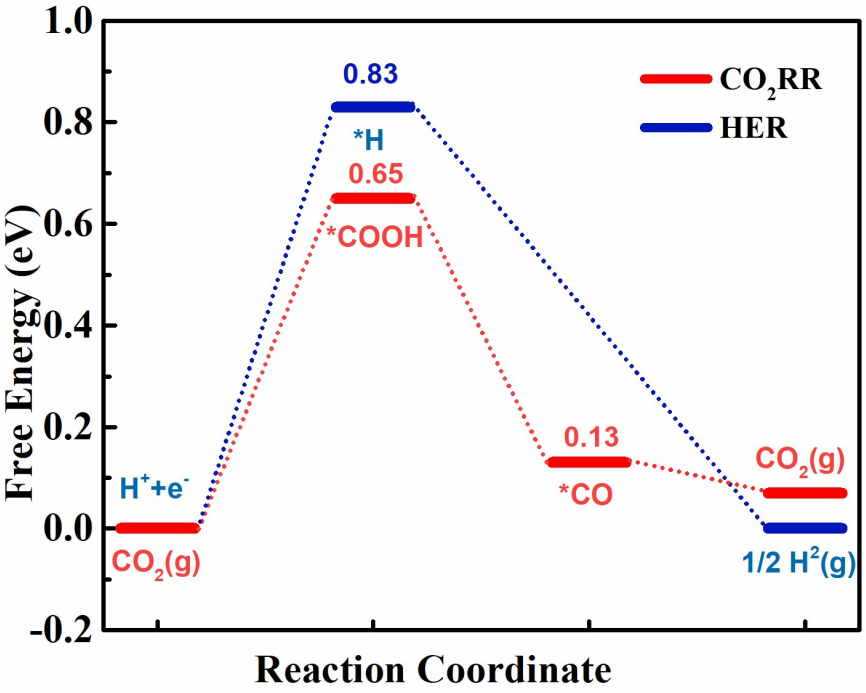

Figure S26. Comparison of the free energy diagram of the Cu-N-C site pathway between CO_2RR and HER at 0 V.

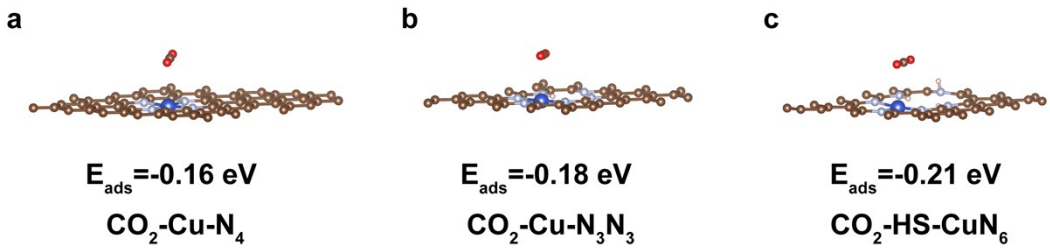

Figure S27. The optimized molecular configuration and calculated adsorption energy of CO_2 on (a) Cu-N_4, (b) Cu-N_3N_3, and (c)HS-CuN_6.

REFERENCES

1 H. Bin Yang, S. F. Hung, S. Liu, K. Yuan, S. Miao, L. Zhang, X. Huang, H. Y. Wang, W. Cai, R. Chen, J. Gao, X. Yang, W. Chen, Y. Huang, H. M. Chen, C. M. Li, T. Zhang and B. Liu, *Nat. Energy*, 2018, **3**, 140–147.

2 C. Yan, H. Li, Y. Ye, H. Wu, F. Cai, R. Si, J. Xiao, S. Miao, S. Xie, F. Yang, Y. Li, G. Wang and X. Bao, *Energy Environ. Sci.*, 2018, **11**, 1204–1210.

3 G. Kresse and J. Furthmüller, *Comput. Mater. Sci.*, 1996, **6**, 15–50.

4 P. E. Blöchl, *Phys. Rev. B*, 1994, **50**, 17953–17979.

5 J. P. Perdew, J. A. Chevary, S. H. Vosko, K. A. Jackson, M. R. Pederson, D. J. Singh and C. Fiolhais, *Phys. Rev. B*, 1993, **48**, 4978.

6 J. D. Pack and H. J. Monkhorst, *Phys. Rev. B*, 1977, **16**, 1748–1749.

7 J. K. Nørskov, T. Bligaard, A. Logadottir, J. R. Kitchin, J. G. Chen, S. Pandelov and U. Stimming, *J. Electrochem. Soc.*, 2005, **152**, J23–J26.

8 E. Skúlason, T. Bligaard, S. Gudmundsdóttir, F. Studt, J. Rossmeisl, F. Abild-Pedersen, T. Vegge, H. Jónsson and J. K. Nørskov, *Phys. Chem. Chem. Phys.*, 2012, **14**, 1235–1245.

9 X. M. Hu, H. H. Hval, E. T. Bjerglund, K. J. Dalgaard, M. R. Madsen, M. M. Pohl, E. Welter, P. Lamagni, K. B. Buhl, M. Bremholm, M. Beller, S. U. Pedersen, T. Skrydstrup and K. Daasbjerg, *ACS Catal.*, 2018, **8**, 6255–6264.

10 E. Zhang, T. Wang, K. Yu, J. Liu, W. Chen, A. Li, H. Rong, R. Lin, S. Ji, X. Zheng, Y. Wang, L. Zheng, C. Chen, D. Wang, J. Zhang and Y. Li, *J. Am. Chem. Soc.*, 2019, **141**, 16569–16573.

11 R. Daiyan, X. Tan, R. Chen, W. H. Saputera, H. A. Tahini, E. Lovell, Y. H. Ng, S. C. Smith, L. Dai, X. Lu and R. Amal, *ACS Energy Lett.*, 2018, **3**, 2292–2298.